Adaptive Normalized Huber Control for Sustainable PV-Integrated Electric Vehicle Chargers with Bidirectional Grid Support

Nitin Kumar[1*] and Mukhtiar Singh[1†]

[1*]Department of Electrical Engineering, D.T.U, Bhawana Road, Delhi, 110042, delhi, India.

*Corresponding author(s). E-mail(s): Ni3sonwal@gmail.com;
Contributing authors: mukhtiarsingh@dce.ac.in;
†These authors contributed equally to this work.

Abstract

Today's global concern is the increase of the earth temperature, to overcome this use of EV and PV has been motivated. This solution has it chalenge also, as to incorporate both PV and EV together in one system. This paper presents an approach to integrate grid-integrated electric vehicle (EV) charging system powered by photovoltaic (PV) using an Adaptive Normalized Huber (ANH) control algorithm. Also, ANH-based control scheme aims to regulate the front-end converter (FEC), which is the first stage of integrated system. In addition, it regulates the DC bus voltage $(\boldsymbol{V_{DC}})$ during the Grid-to-vehicle (G2V) and Vehicle-to-Grid (V2G) modes of operation. Hardware results proves the efficacy of the proposed control scheme under dynamic conditions, demonstrating a source current THD of 4.9% and rapid transient recovery within two cycles. Comparative analysis with conventional Least Mean Square (LMS) and Second-Order Generalized Integrator (SOGI) filters confirms superior tracking speed and robustness of the ANH controller.

Keywords: wireless power transfer (WPT Inductive Power transfer (IPT), Electric Vehicle Charging (EV), HFAC, Wireless EV charging, Coil Designs, Inductive Coupling

R. Vasanth Kumar Mehta et al. (eds.), *Proceedings of the International Conference on Intelligent Systems for a Sustainable Future (ISSF 2026)*, Atlantis Highlights in Intelligent Systems 16,
https://doi.org/10.2991/978-94-6239-693-7_43

1 Introduction

increasing growth of distributed generation (DG) techniques has leads to the adoption of microgrids as sustainable alternatives & reliable to conventional centralized power systems. In the underdeveloped regions or the hilly regions, continuity of the power supply is the challenge, so microgrids best choice, which are capable of working in both grid-connected and islanding mode. The integration of renewable energy sources, such as photovoltaic (PV) arrays and wind systems, has become an important component of these networks. Among these, PV-based generation is particularly appealing due to its modularity, environmental compatibility, and low operational cost. However, the intermittent and nonlinear nature of solar energy introduces challenges in maintaining power quality and stable grid interaction, especially when giving power to non-linear loads which are connected at the point of common coupling (PCC). [1, 2].

Henceforth, to reduce these intermittent, battery energy storage system (BESS) are integrated into PV-connected microgrids. Therefore, this arrangement will allow the excess power to be stored during peak generation and released during duration of low irradiance [3]. This results in voltage and frequency stability while maintaining the balance between supply and demand. Also, the Front end converter (FEC) and DC/DC converter plays an important role in the interface of renewable & storage elements with the grid. Stabilizing DC bus voltage and achieving sinusoidal grid current under non-linear load conditions at the point of common coupling (PCC) remain key control challenges [4, 5].

Conventional control strategies like Least Mean Square (LMS), least mean forth (LMF) & Second-Order Generalized Integrator (SOGI) algorithms have been used widely for fundamental extraction and harmonic compensation [6, 7]. But, these methods are too sensitive to noise, convergence rates are slow, and give the degraded performance when subjected to non-ideal grid conditions. On the other hand, adaptive control algorithms are so robust that they dynamically tune their parameters to have the faster response and improved efficency. Recently, researchers have explored advanced adaptive filtering and optimization-based methods to address PQ disturbances in nonlinear systems [8, 9]. However, many of these increases either increases computational complexity or fail to maintain steady-state accuracy under parameter uncertainties.

Further, to curtail the problems discussed in above paragraph, this paper present an Adaptive Normalized Huber (ANH) control algorithm for a 1ph PV–Battery integrated system. The proposed control scheme combines the characteristics of Huber loss-based robustness with adaptive normalization to improve the stability of convergence and reduce sensitivity to outliers [10, 11]. By precisely estimating the fundamental component of the nonlinear load current, the ANH algorithm generates accurate reference currents for the FEC, which leads to compensate the harmonics and regulate the DC bus voltage.

The technical contribution of this research is as follows:

- Development of an Adaptive Normalized Huber (ANH) controller for a PV–Battery integrated VSC to enhance power quality and system stability.

- Real-time regulation of DC-link voltage and harmonic suppression under nonlinear and dynamic load variations.
- Implementation of bidirectional DC–DC and boost converters for coordinated PV generation and battery storage management.
- Experimental validation and comparative evaluation with LMS and SOGI algorithms confirming improved tracking accuracy and faster convergence.

The remaining structure of the paper is as follows: Section II states the description of the system. The mathematical analysis of the proposed ANH controller is described in Section III. Section IV states the overall control of the system. The experimental results are discussed in Section V. Finally, Section VI concludes the paper.

2 System Configuration

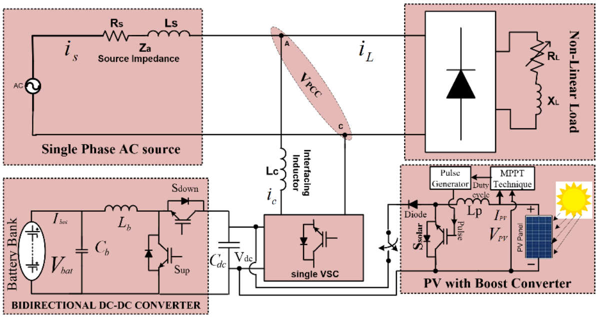

Fig. 1 Configuration of the proposed single-phase PV–Battery integrated VSC system feeding a nonlinear load.

Figure 1 shows the configuration of the proposed single-phase PV–Battery integrated system employing a Voltage Source Converter (VSC) for power quality improvement under nonlinear load conditions. The system consists of a single-phase AC source represented by source impedance ($R_s + j\omega L_s$) supplying a nonlinear load through the Point of Common Coupling (PCC). The nonlinear load, modeled using a diode bridge with an R_L–X_L network, introduces current distortion into the grid. A VSC interfaced through an inductor (L_c) is employed to inject compensating currents (i_c), thereby maintaining the source current (i_s) sinusoidal and in phase with the supply voltage. The DC-link capacitor (C_{dc}) is regulated by a bidirectional DC–DC converter connected to a battery bank (V_{bat}, I_{bat}), which supports both charging and discharging operations to balance power flow.

3 Adaptive Normalized Huber (ANH) Control Scheme

3.1 Load Current Decomposition

$$i_L(t) = I_1 \sin(\omega t + \theta_1) + \sum_{m=2}^{\infty} I_m \sin(m\omega t + \theta_m) \tag{1}$$

Expanding (1) gives:

$$i_L(t) = \sum_{m=1,3,5,\dots}^{\infty} \big[a_m \sin(m\omega t) + b_m \cos(m\omega t)\big] \tag{2}$$

where $a_m = I_m \cos(\theta_m)$ and $b_m = I_m \sin(\theta_m)$.

3.2 Vectorized Representation

Equation (2) can be expressed in vector form as:

$$i_L(t) = \phi^T(t) w(n) \tag{3}$$

where

$$\phi(t) = [\sin(\omega t), \cos(\omega t), \sin(3\omega t), \cos(3\omega t), \dots]^T,$$

and

$$w(n) = [a_1, b_1, a_3, b_3, \dots]^T.$$

3.3 Instantaneous Error and Huber Cost

The prediction error between the measured and estimated load current is:

$$e(n) = i_L(n) - \phi^T(n) w(n-1) \tag{4}$$

To achieve robustness against large disturbances, the Huber cost function is used:

$$J(n) = \begin{cases} \frac{1}{2} e^2(n), & |e(n)| \le \Delta, \\ \Delta |e(n)| - \frac{1}{2}\Delta^2, & |e(n)| > \Delta, \end{cases} \tag{5}$$

where Δ is the transition threshold between quadratic and linear regions.

3.4 Adaptive Weight Update Law

Minimizing the cost function with respect to $w(n)$ gives:

$$w(n+1) = w(n) + \mu \frac{\psi(n)\phi(n)}{\varepsilon + \|\phi(n)\|^2} \tag{6}$$

where μ is the adaptation gain, ε is a small positive constant for stability, and

$$\psi(n) = \begin{cases} e(n), & |e(n)| \leq \Delta, \\ \Delta\, \mathrm{sign}[e(n)], & |e(n)| > \Delta. \end{cases} \tag{7}$$

3.5 Fundamental Component Reconstruction

Once $w(n)$ converges, the estimated fundamental current is reconstructed as:

$$\hat{i}_1(t) = \phi_1^T(t) w_1(n), \tag{8}$$

where $\phi_1(t) = [\sin(\omega t), \cos(\omega t)]^T$. The compensating reference current for the converter is:

$$i_{\mathrm{ref}}(t) = \hat{i}_1(t) + i_{\mathrm{dc}}(t) \tag{9}$$

where $i_{\mathrm{dc}}(t)$ maintains the DC-link voltage.

3.6 Stability Criterion

The ANH control law ensures stability when:

$$\Delta J(n) = J(n+1) - J(n) < 0, \quad \forall n, \tag{10}$$

which holds if

$$0 < \mu < \frac{2}{\lambda_{\max}(R)},$$

where $\lambda_{\max}(R)$ is the maximum eigenvalue of the input correlation matrix $R = E[\phi(n)\phi^T(n)]$.

In the proposed control framework, the estimation of the fundamental active power weight component w_n of the load current is governed by the adaptive update law described in Eq. (10), which is triggered when $|e(n)| > k$. The control parameters $\gamma = 0.005$ and $\sigma = 0.1$ were selected through simulation-based optimization to achieve the most favorable dynamic response and steady-state performance. Unlike conventional adaptive algorithms such as the Least Mean Square (LMS) method that primarily aim to minimize the mean square error, the proposed Adaptive Normalized Huber (ANH) control algorithm employs an advanced adaptive filtering approach designed to minimize instantaneous error with improved robustness against noise and system disturbances. As depicted in Fig. 2, the ANH controller continuously updates the adaptive weight w_n to w_{n+1} in each iteration based on variations in the measured load current i_L, the weight signal, and the unit reference template $u(n)$, effectively reducing the instantaneous error $e(n)$.

The Adaptive Normalized Huber (ANH) weight update algorithm is employed within the system controller to extract the fundamental active component of the load current. This mechanism is implemented in a single-phase full-bridge Voltage Source Converter (VSC) to ensure precise injection of compensating currents at the Point of Common Coupling (PCC).

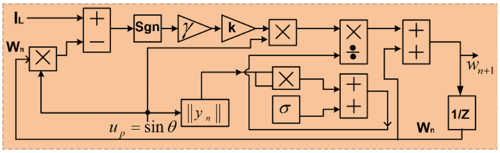

Fig. 2 Circuit diagram of ANH

4 Overall control scheme for PV-Battery Integrated System

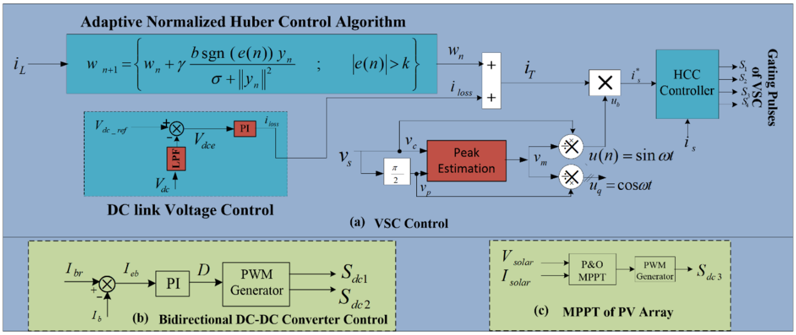

Fig. 3 Control Diagram of the complete system

4.1 Overview

Fig. 3 illustrates the comprehensive control architecture of the proposed Adaptive Normalized Huber (ANH) based Voltage Source Converter (VSC) system. The scheme combines three coordinated modules:

1. VSC control using the ANH algorithm,
2. DC-link voltage regulation, and
3. Energy management via bidirectional DC–DC converter and PV maximum power point tracking (MPPT).

4.2 VSC Control Using ANH Algorithm

The upper section of Fig. 3(a) represents the main VSC control loop governed by the ANH adaptation law. The instantaneous nonlinear load current i_L is processed through the ANH estimator to extract the fundamental component while suppressing higher-order harmonics.

The adaptive weight update rule is defined as:

$$w_{n+1} = \begin{cases} w_n + \dfrac{b\,\mathrm{sgn}(e(n))\,y_n}{\sigma + \|y_n\|^2}, & |e(n)| > k, \\ w_n + \gamma \dfrac{e(n)\,y_n}{\sigma + \|y_n\|^2}, & |e(n)| \le k, \end{cases} \tag{11}$$

where $e(n)$ is the estimation error, y_n is the input reference vector, and the constants b, γ, and σ determine the adaptive step size and normalization. The updated weight vector w_{n+1} yields the estimated fundamental component current.

The resultant reference current is formed as:

$$i_T = \hat{i}_1 + i_{\mathrm{loss}}, \tag{12}$$

where i_{loss} is the compensating current obtained from DC-link voltage control. The total current i_T is fed to a Hysteresis Current Controller (HCC), which produces the gating signals $(S_1, S_2, S_{1'}, S_{2'})$ for the VSC switches to ensure fast current tracking and minimal distortion.

The Peak Estimation block extracts the unit voltage templates $u_p = \cos\omega t$ and $u_q = \sin\omega t$ from the supply voltage v_s, ensuring the supply current is in phase with the voltage for unity power factor operation.

4.3 DC-Link Voltage Regulation

The DC-link voltage control loop maintains the desired DC bus voltage across the VSC as depicted in Fig. 3(a). The measured voltage V_{dc} is compared with its reference V_{dc_ref}, and the error is passed through a Low-Pass Filter (LPF) to remove switching ripples. The filtered signal is then processed by a PI controller:

$$i_{\mathrm{loss}} = K_p(V_{dc\_ref} - V_{dc}) + K_i \int (V_{dc\_ref} - V_{dc})\,dt, \tag{13}$$

where K_p and K_i are proportional and integral gains, respectively. The output i_{loss} compensates converter power losses and maintains DC-link voltage stability during transient and steady-state conditions.

4.4 Bidirectional DC–DC Converter Control

The bidirectional DC–DC converter, shown in Fig. 3(b), manages energy exchange between the battery and the DC-link. Depending on the grid and PV conditions, it operates in:

- Boost (Discharging) mode: when the battery supplies power to the DC-link, and
- Buck (Charging) mode: when excess energy charges the battery.

The current error $(I_{br} - I_b)$ is passed through the PI regulator to generate the duty ratio D. The corresponding PWM pulses (S_{dc1}, S_{dc2}) are applied to control the bidirectional converter switches, ensuring smooth energy flow and battery protection.

4.5 MPPT Control of PV Array

The Fig. 3(c) represents the Maximum Power Point Tracking (MPPT) of the PV array. The PV voltage V_{solar} and current I_{solar} are measured and fed to the Perturb-and-Observe (P&O) algorithm to extract maximum available power.

4.6 Integrated System Performance

The coordinated operation of the three loops enables:

- Accurate extraction of the fundamental current component using the ANH estimator,
- Maintenance of constant DC-link voltage through the PI–LPF control mechanism,
- Efficient bidirectional power transfer between PV, battery, and grid, and
- Reduction in total harmonic distortion (THD) with improved power quality and dynamic stability.

4.7 Technical Significance

The ANH algorithm combines the robustness of the Huber function with the stability of normalized adaptation, providing robustness against noise and the nonlinearity at the PCC. Compared with conventional LMS or NLMS algorithms, the proposed controller demonstrates superior convergence speed, harmonic suppression capability, and immunity to grid disturbances, making it suitable for the proposed systems.

5 Results and Discussion

A hardware prototype model is made in the laboratory. Three current sensors (LA-25P) were used to measure source current (is), load current (iL), and battery current (Ibat), and three voltage sensors (LV-25P) were used to measure source voltage (vs), DC link voltage (Vdc), and battery voltage (Vbat). All sensor output is received via the Analogue to Digital Channel (ADC) of the dSpace 1104. The dSpace 1104 controller generates the two pulses for the bidirectional DC-DC converter and the four gating pulses for the FEC.

The performance of the proposed Adaptive Normalized Huber (ANH) controller is validated experimentally on a PV–Battery-supported Voltage Source Converter (VSC) prototype. The controller performance is evaluated under two distinct operating modes: battery charging and battery discharging.

5.1 Battery Charging Mode

During the charging period, the bidirectional DC–DC converter operates in buck mode, drawing excess energy from the grid or PV source to charge the battery bank while maintaining the DC-link voltage. The ANH controller ensures sinusoidal grid current and unity power factor operation.

5.1.1 Power Analyzer Observations

Figure 4 presents the power analyzer readings for battery charging mode. The analyzer displays RMS voltage, RMS current, active power, apparent power, reactive power, and power factor during steady-state operation.

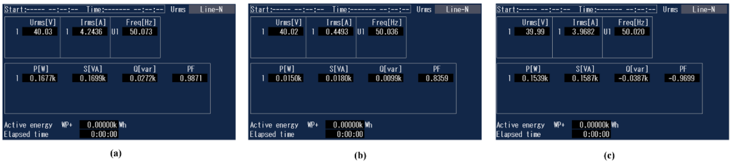

(a)

Start:----- --:--:-- Time:------- --:--:-- Urms Line-N
Urms[V] 1 40.03
Irms[A] 1 4.2436
Freq[Hz] U1 50.073
P[W] 1 0.1677k
S[VA] 0.1699k
Q[var] 0.0272k
PF 0.9871
Active energy WP+ 0.00000k Wh
Elapsed time 0:00:00

(b)

Start:----- --:--:-- Time:------- --:--:-- Urms Line-N
Urms[V] 1 40.02
Irms[A] 1 0.4493
Freq[Hz] U1 50.036
P[W] 1 0.0150k
S[VA] 0.0180k
Q[var] 0.0099k
PF 0.8359
Active energy WP+ 0.00000k Wh
Elapsed time 0:00:00

(c)

Start:----- --:--:-- Time:------- --:--:-- Urms Line-N
Urms[V] 1 39.99
Irms[A] 1 3.9682
Freq[Hz] U1 50.020
P[W] 1 0.1539k
S[VA] 0.1587k
Q[var] -0.0387k
PF -0.9699
Active energy WP+ 0.00000k Wh
Elapsed time 0:00:00

Fig. 4 Power analyzer readings during battery charging mode
: (a) grid-side, (b) PV-side, (c) converter-side measurements.

As observed, the RMS voltage remains nearly constant at 40 V while the RMS current is approximately 0.45 A. The active power recorded is around 15 W with a power factor of 0.835. The system thus draws small active power from the grid to charge the battery. The low reactive power ($Q = 9.9$ var) and unity-aligned current indicate that the ANH algorithm effectively maintains a sinusoidal current profile during energy absorption.

5.1.2 DSO Waveforms

The DSO-captured results for the charging operation are shown in Fig. 5. The top waveform represents the grid voltage and current, while the subsequent traces correspond to load and converter currents.

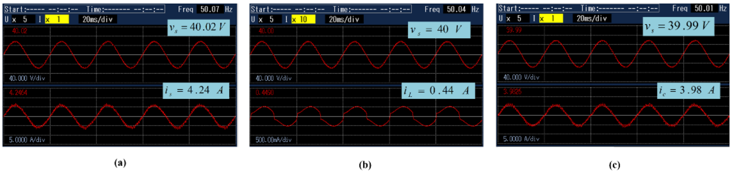

Fig. 5 DSO waveforms during battery charging mode
: (a) grid voltage and current (v_s, i_s), (b) load current (i_L), (c) converter current (i_c).

It can be noted that the supply voltage and current (v_s, i_s) are in phase, confirming unity power factor operation. The measured values are $v_s = 40.02$ V and $i_s = 4.24$ A with a switching frequency of 50 Hz. The converter injects an active current of $i_c = 3.98$ A in phase with the supply voltage, while the load current ($i_L = 0.44$ A) remains minimal due to light loading. These results validate efficient charging with low current distortion.

5.1.3 Dynamic Performance During Load Variation

To verify transient behavior, a load-decrease test is performed during the charging period. The corresponding results are presented in Fig. 6. The waveforms display the DC-link voltage (V_{dc}), load current (i_L), reference current (i_{ref}), and battery current (i_{bat}).

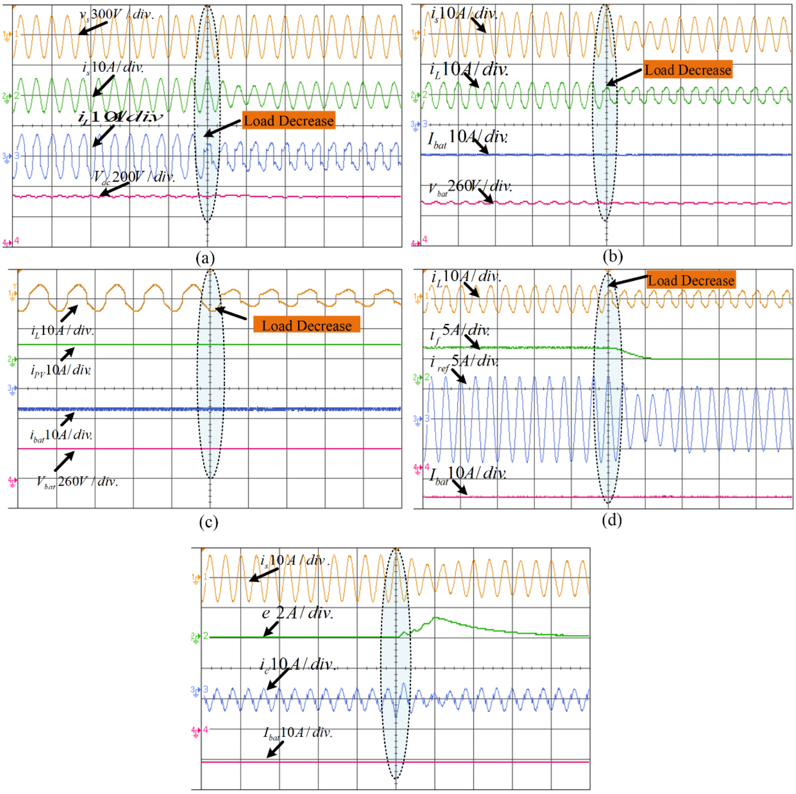

Fig. 6 Dynamic response of the system under load variation in charging mode

.

the supply current immediately decreases when there is a decrese in load, while maintaining waveform symmetry. The DC bus voltage exhibits a small transient before manitaining itself to a reference value of 260 V. The battery current (i_{bat}) smoothly transitions without overshoot, confirming the ANH controller's robust tracking and damping characteristics. Thus, under load perturbations, the system remains stable and maintains effective power management.

5.1.4 Summary

The charging-mode performance validates that:

- The ANH controller ensures near-unity power factor and harmonic suppression.
- The DC-link voltage is well regulated during dynamic load change.
- The battery charging current transitions smoothly, avoiding oscillations.

Hence, the system exhibits robust, distortion-free grid interaction during charging operation.

5.2 Battery Discharging Mode

In discharging mode also known as Vehicle to grid (V2G), the bidirectional converter works as a boost mode. Therefore, the stored battery energy is released through the DC bus voltage and supplied to the grid. The ANH algorithm helps in mainting the sinusoidal current injection with little distortion.

5.2.1 Power Analyzer Observations

The power analyzer results during Vehicle to grid or discharging are depicted in Fig. 7. The Root Mean Square values of grid voltage is 41.75 V, grid current is 2.41 A, and the active power observed to be approx. 99 W, with a power factor of −0.987.

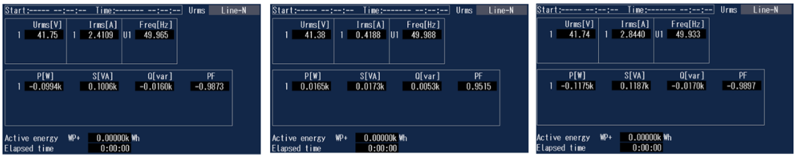

```
Start:----- --:--:--  Time:------- --:--:--  Urms  Line-N
   Urms[V]       Irms[A]       Freq[Hz]
 1  41.75     1  2.4109    U1  49.965

     P[W]         S[VA]        Q[var]        PF
 1 -0.0994k     0.1006k      -0.0160k     -0.9873

Active energy  WP+  0.00000k Wh
Elapsed time         0:00:00
```

(a)

```
Start:----- --:--:--  Time:------- --:--:--  Urms  Line-N
   Urms[V]       Irms[A]       Freq[Hz]
 1  41.38     1  0.4188    U1  49.988

     P[W]         S[VA]        Q[var]        PF
 1  0.0165k     0.0173k       0.0053k      0.9515

Active energy  WP+  0.00000k Wh
Elapsed time         0:00:00
```

(b)

```
Start:----- --:--:--  Time:------- --:--:--  Urms  Line-N
   Urms[V]       Irms[A]       Freq[Hz]
 1  41.74     1  2.8440    U1  49.933

     P[W]         S[VA]        Q[var]        PF
 1 -0.1175k     0.1187k      -0.0170k     -0.9897

Active energy  WP+  0.00000k Wh
Elapsed time         0:00:00
```

(c)

Fig. 7 Power analyzer readings during battery discharging mode
: (a) grid-side, (b) PV-side, (c) converter-side measurements.

The negative sign of the power factor confirms reverse active power flow from the battery to the grid, indicating successful discharging. The apparent power ($S = 100.6$ VA) and low reactive power ($Q = 16$ var) demonstrate high efficiency and excellent phase alignment between voltage and current.

5.2.2 DSO Waveforms

The Digital signal Oscilloscope results in corresponding to the vehicle to grid or discharging operation as shown in Fig. 8. The sinusoidal nature of (v_s) and (i_s) waveforms confirm that the converter deliver active power back to the grid with samll harmonic content.

Here, $v_s = 41.33$ V and $i_s = 2.44$ A shows the in-phase and sinusoidal nature, while the converter current $i_c = 2.84$ A shows reverse polarity in terms of the supply current, reflecting the power back into the grid. The gird current waveform observed to be smooth and sinusoidalal, which proves the efficacy of the controller.

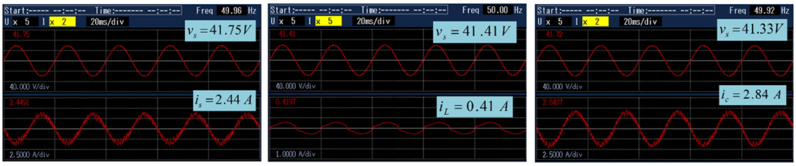

(a) (b) (c)

Fig. 8 DSO waveforms during battery discharging mode

: (a) supply voltage and current (v_s, i_s), (b) load current (i_L), and (c) converter current (i_c).

5.2.3 Dynamic Performance During Load Variation

Figure 9 depicts the dynamic response during a load decrease in V2G mode. The results show stable operation with slight transient deviation.

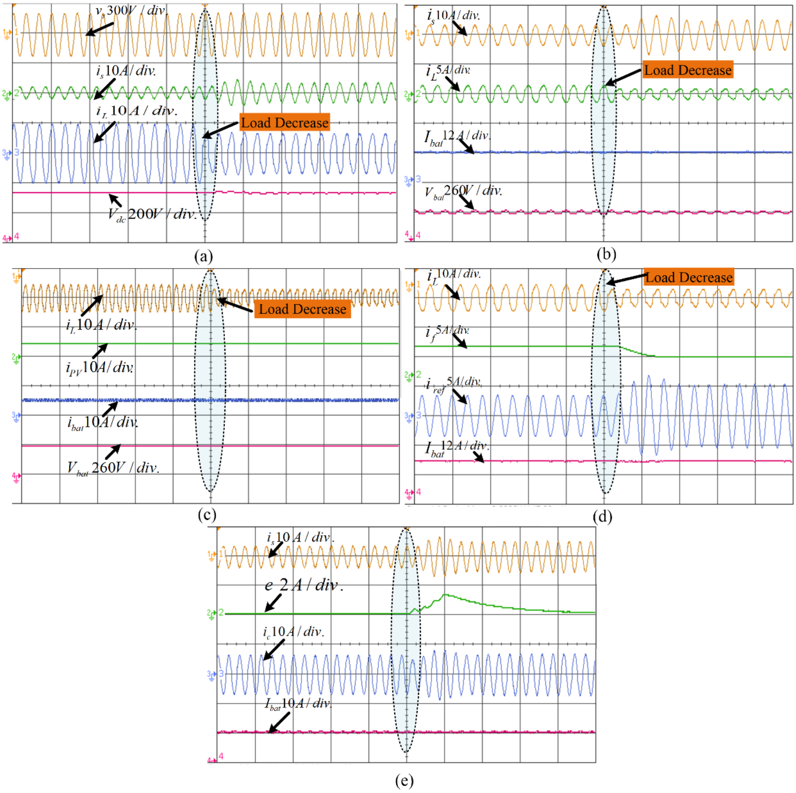

Fig. 9 Dynamic response of system under load variation in the discharging mode

.

Therefore, the DC bus voltage (V_{dc}) remains undisturbed at 260 V even under the load dynamics as depicted. The grid current and the compensating current waveforms shows smooth adjustment without overshoot. The proposed controller ensures a constant current injection and reliable tracking during the load changes.

5.2.4 Summary

Under discharging conditions, the system achieves:

- Stable reverse power flow with unity power factor.
- Well-regulated DC-link voltage under varying load.
- Distortion-free sinusoidal grid current confirming ANH controller effectiveness.

5.3 Overall System Performance

The experimental results confirm that the proposed ANH control strategy successfully coordinates the PV–Battery–VSC interface. Both charging and discharging operations exhibit:

- Robust transient response with stable DC-link regulation.
- Sinusoidal grid current with minimal THD.
- Reliable bidirectional energy flow between battery and grid.

Hence, the ANH-based control provides superior performance in grid-tied renewable systems under nonlinear and dynamic operating conditions.

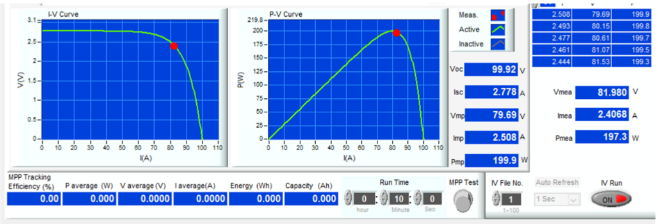

2.508	79.69	199.9
2.493	80.15	199.8
2.477	80.61	199.7
2.461	81.07	199.5
2.444	81.53	199.3

Voc 99.92 V
Isc 2.778 A
Vmp 79.69 V
Imp 2.508 A
Pmp 199.9 W
Vmea 81.980 V
Imea 2.4068 A
Pmea 197.3 W

MPP Tracking Efficiency (%)	P average (W)	V average (V)	I average(A)	Energy (Wh)	Capacity (Ah)
0.00	0.000	0.0000	0.0000	0.000	0.000

Run Time 0 hour : 10 Minute : 0 Sec
IV File No. 1 (1~100)
1 Sec

Fig. 10 Trace of MPPT on PV Simulator

Fig. 10 shows that the PV simulator injects 200W power to support the grid, load, and battery.

5.4 Comparative Performance of Fundamental Component Extraction

Fig. 11 depicts the comparison analysis of convectional algorithm to extract fundamental component like, LMS, SOGI, and the proposed ANH, under a non-linear load condition. The LMS algorithm shows the slow convergence and pronounced ripple, indicating too sensitivity to harmonics and the noise. On the other hand, SOGI method depicts the moderate improved stability but still suffers from steady-state error under dynamic behaviour of load. Henceforth, the proposed algorithm shows the

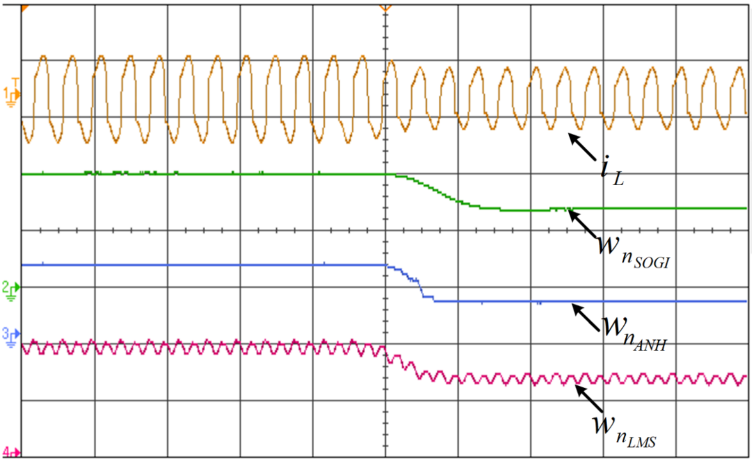

Fig. 11 Comparison of adaptive weight convergence for different algorithms under nonlinear load: LMS, SOGI, and proposed ANH.

fastest convergence with very less ripple and high robustness against measurement noise. Its adaptive normalization mechanism ensures accurate and stable extraction of the fundamental current component even under highly distorted conditions.

6 Conclusion

A renewable energy-based electric vehicle charging system based on the Adaptive Normalized Huber (ANH) control algorithm has been experimentally modeled and verified. The proposed controller ensures robustness in bidirectional power-flow management, harmonic reduction, and stability across both G2V/V2G modes, achieving THD less than 5 % as IEEE standards. Furthermore, by integrating PV-EV system, an adaptive converter control demonstrates an effective pathway for sustainable electric mobility. At last, a comparison between LMS and SOGI control methods proves that ANH shows faster convergence, lower steady-state error, and higher resilience against grid disturbances.

References

[1] Hassan Q, Algburi S, Sameen A Z, Salman H M, and Jaszczur M 2023, "A review of hybrid renewable energy systems: Solar and wind-powered solutions: Challenges, opportunities, and policy implications," *Results in Engineering*, pp. 101621.

[2] Singh Y, Singh B, and Mishra S 2022, "Control of single-phase distributed PV-battery microgrid for smooth mode transition with improved power quality," *IEEE Transactions on Industry Applications*, vol. 58, no. 5, pp. 6286–6296.

[3] Yadav G and Yegon P 2025, "ML-based grid-interactive EV chargers under non-grid conditions," *Applied Computational Intelligence and Soft Computing*, Article ID 1731177, 16 pages.

[4] Gogoi D, Bharatee A, and Ray P K 2024, "Implementation of battery storage system in a solar PV-based EV charging station," *Electric Power Systems Research*.

[5] Yadav G 2025, "Efficient response enhancement under nonideal grid voltage conditions using fourth-order D-QSG–based control grid-interactive EV chargers," *International Journal of Circuit Theory and Applications*, pp. 1–15.

[6] Al-Quraan A, and Al-Qaisi M 2021, "Modelling, Design and Control of a Standalone Hybrid PV-Wind Micro-Grid System," *Energies*.

[7] Yadav G, Mittal S, and Kundu S 2025, "Machine learning-based grid-interactive chargers for optimizing power quality under non-grid conditions," *Hybrid Renewable Power Infrastructure for Sustainable Electric Vehicle Development*, *Studies in Infrastructure and Control*, Springer, Singapore.

[8] Lu S, and Wang X 2019, "Observer-Based Command Filtered Adaptive Neural Network Tracking Control for Fractional-Order Chaotic PMSM," *IEEE Access*, vol. 7, pp. 88777–88788.

[9] Bag A, Subudhi B, and Ray P K 2020, "An Adaptive Variable Leaky Least Mean Square Control Scheme for Grid Integration of a PV System," *IEEE Transactions on Sustainable Energy*, vol. 11, no. 3, pp. 1508–1515.

[10] Yadav G 2025, "Enhancing power quality and stability in grid-interactive electric vehicle chargers using advanced control strategies and disturbance compensation," *Engineering Research Express*, vol. 7, no. 3, article ID 035321.

[11] Sivakumar M, Kannan P, and Pandian S C 2019, "Mitigation of PQ issues using an enhanced UPQC-based ANN approach," *Journal of Circuits, Systems and Computers*, vol. 28, no. 03, pp. 1950046.